PHYSICAL REVIEW B **98**, 045110 (2018)

Time evolution of an infinite projected entangled pair state: An algorithm from first principles

Piotr Czarnik[1] and Jacek Dziarmaga[2]
[1] *Institute of Nuclear Physics, Polish Academy of Sciences, Radzikowskiego 152, PL-31342 Kraków, Poland*
[2] *Institute of Physics, Jagiellonian University, Łojasiewicza 11, PL-30348 Kraków, Poland*

(Received 16 April 2018; revised manuscript received 20 June 2018; published 6 July 2018)

A typical quantum state obeying the area law for entanglement on an infinite two-dimensional (2D) lattice can be represented by a tensor network *Ansatz*, known as an infinite projected entangled pair state (iPEPS), with a finite bond dimension D. Its real-imaginary time evolution can be split into small time steps. An application of a time step generates a new iPEPS with a bond dimension k times the original one. The new iPEPS does not make optimal use of its enlarged bond dimension kD; hence, in principle, it can be represented accurately by a more compact *Ansatz*, preferably with the original D. In this work we show how the more compact iPEPS can be optimized variationally to maximize its overlap with the new iPEPS. To compute the overlap we use the corner-transfer-matrix renormalization group. By simulating sudden quench of the transverse field in the 2D quantum Ising model with the proposed algorithm, we provide a proof of principle that real-time evolution can be simulated with iPEPS. A similar proof is provided with the same model for imaginary-time evolution of purification of its thermal states.

DOI: 10.1103/PhysRevB.98.045110

I. INTRODUCTION

Tensor networks are a natural language to represent quantum states of strongly correlated systems [1,2]. Among them the most widely used *Ansätze* are a matrix product state (MPS) [3] and its two-dimensional (2D) generalization: the projected entangled pair state (PEPS) [4], also known as a tensor product state. Both obey the area law for entanglement entropy. In one dimension matrix product states are efficient parametrizations of ground states of gapped local Hamiltonians [1,5,6] and purifications of thermal states of one-dimensional (1D) local Hamiltonians [7]. MPS is the *Ansatz* optimized by the density-matrix renormalization group (DMRG) [8,9], which is one of the most powerful methods to simulate not only ground states of 1D systems but also their exited states, thermal states, and dynamic properties [10,11].

PEPSs are expected to be an efficient parametrization of ground states of 2D gapped local Hamiltonians [1,2] and were shown to be an efficient representation of thermal states of 2D local Hamiltonians [12], although in two dimensions there are limitations to the assumed representability of area-law states by tensor networks [13]. Furthermore, tensor networks can be used to represent efficiently systems with fermionic degrees of freedom [14–17], which was demonstrated for both finite [18] and infinite PEPSs [19,20].

PEPS was originally proposed as a variational *Ansatz* for ground states of 2D finite systems [4,21], generalizing earlier attempts to construct trial wave functions for specific 2D models using 2D tensor networks [22]. Efficient numerical methods enabling optimization and controlled approximate contraction of an infinite PEPS (iPEPS) [23–26] became the basis for promising new methods for strongly correlated systems. Among the recent achievements of those methods are the solution of a long-standing magnetization plateau problem in the highly frustrated compound $SrCu_2(BO_3)_2$ [27,28] and obtaining the coexistence of superconductivity and striped order in the underdoped regime of the Hubbard model, a result which is corroborated by other numerical methods (among them is another tensor network approach, DMRG simulations of finite-width cylinders), apparently settling one of the long-standing controversies concerning that model [29]. Another example of a recent contribution of iPEPS-based methods to condensed-matter physics is the problem of the existence and nature of the spin-liquid phase in the kagome Heisenberg antiferromagnet for which new evidence in support of a gapless spin liquid was obtained [30]. This progress was accompanied and partly made possible by new developments in iPEPS optimization [31,32], iPEPS contraction [33–35], energy extrapolations [36], and universality-class estimation [37–39]. These achievements encourage attempts to use iPEPS to simulate the broad class of states obeying the 2D area-law-like thermal states [35,40–46], states of dissipative systems [47], and exited states [48].

Among alternative tensor network approaches to strongly correlated systems are methods of direct contraction and renormalization of a three-dimensional tensor network representing a density operator of a 2D thermal state [49–55] and the multiscale entanglement renormalization *Ansatz* (MERA) [56,57], which is technically challenging yet able to represent critical states with subleading logarithmic corrections to the area law, and its generalization, the branching MERA [58,59]. Progress in using DMRG to simulate cylinders with finite width has also been made in recent years. Such simulations are routinely used alongside iPEPS to investigate 2D system ground states (see, e.g., Ref. [29]) and were applied recently to thermal states [60,61].

In this work we test an algorithm to simulate either real- or imaginary-time evolution with iPEPS. The algorithm uses second-order Suzuki-Trotter decomposition of the evolution operator into small time steps [62–64]. A straightforward application of a time step creates a new iPEPS with a bond dimension k times the original bond dimension D. If not truncated, the evolution would result in an exponential growth of the bond dimension. Therefore, the new iPEPS is approximated variationally by an iPEPS with the original D. The algorithm is a straightforward construction direct from first principles with a minimal number of approximations controlled by the iPEPS bond dimension D and the environmental bond dimension χ in the corner-transfer-matrix renormalization group (CTMRG). It uses CTMRG [26,65–67] to compute the fidelity between the new iPEPS and its variational approximation. The calculation of fidelity between two close iPEPSs was shown to be tractable only very recently [68]. In this work we go further and demonstrate that the fidelity can be optimized variationally effectively enough for time evolution.

A challenging application of the method is real-time evolution after a sudden quench. A sudden quench of a parameter in a Hamiltonian excites entangled pairs of quasiparticles with opposite quasimomenta that move away from each other crossing the boundary of the subsystem. Consequently, the number of pairs that are entangled across the boundary (proportional to the entanglement entropy) grows linearly with time, requiring an exponential growth of the bond dimension. Therefore, a tensor network is doomed to fail after a finite evolution time. Nevertheless, matrix product states proved to be useful for simulating time evolution after sudden quenches in one dimension [69]. As a proof of principle that the same can be attempted with iPEPS in two dimensions, in this work we simulate a sudden quench in the transverse field quantum Ising model.

Moreover, there are other (easier from the entanglement point of view) potential applications of the real-time variational evolution. For instance, a smooth ramp of a parameter in a Hamiltonian across a quantum critical point generates the entanglement entropy proportional to the area of the boundary times a logarithm of the Kibble-Zurek correlation length $\hat{\xi}$ that, in turn, is a power of the ramp time [70]. Thanks to this dynamical area law, the required D instead of growing exponentially with time saturates, becoming a power of the ramp time. Even stronger limitations may apply in many-body localization (MBL), where localized excitations are not able to spread the entanglement. Tensor networks have already been applied to 2D MBL phenomena [71]. Finally, after vectorization of the density matrix, the unitary time evolution can be generalized to a Markovian master equation with a Lindblad superoperator, where local decoherence limits the entanglement, making the time evolution with a tensor network feasible [47,72].

Another promising application is imaginary-time evolution generating thermal states of a quantum Hamiltonian. By definition, a thermal Gibbs state maximizes entropy for a given average energy. As this maximal entropy is the entropy of entanglement of the system with the rest of the universe, then by the monogamy of entanglement, there is little entanglement left inside the system. In more quantitative terms, both thermal states of local Hamiltonians and iPEPS representations of density operators obey the area law for mutual information, making an iPEPS a good *Ansatz* for thermal states [73]. In this paper we evolve a purification of thermal states in the quantum Ising model, obtaining results convergent to the variational tensor network renormalization (VTNR) introduced and applied to a number of models in [35,43–45]. This test is a proof of principle that thermal states can be obtained with the variational imaginary-time evolution.

This paper is organized as follows. In Sec. II we introduce the purification of a thermal state to be evolved in imaginary time. In Sec. III we introduce the algorithm in the more general case of imaginary-time evolution of a thermal-state purification. A modification to real-time evolution of a pure state is straightforward. In Sec. III A we show Suzuki-Trotter decomposition of a small time step and represent it by a tensor network. In Sec. III B we outline the algorithm, whose further details are refined in Secs. III C, III D, and the Appendix. In Sec. IV the algorithm is applied to simulate imaginary-time evolution generating thermal states. The results are compared with VTNR. In Sec. V the real-time version of the algorithm is tested in the challenging problem of time evolution after a sudden quench. Finally, we conclude in Sec. VI.

II. PURIFICATION OF THERMAL STATES

We will exemplify the general idea with the transverse field quantum Ising model on an infinite square lattice

$$H = -\sum_{\langle j,j'\rangle} Z_j Z_{j'} - \sum_j (h_x X_j + h_z Z_j). \tag{1}$$

Here Z, X are Pauli matrices. At zero longitudinal bias, $h_z = 0$, the model has a ferromagnetic phase with a nonzero spontaneous magnetization $\langle Z\rangle$ for sufficiently small transverse field h_x and sufficiently large inverse temperature β. At $h_x = 0$ the critical β is $\beta_0 = -\ln(\sqrt{2}-1)/2 \approx 0.441$, and at zero temperature the quantum critical point is $h_0 = 3.04438(2)$ [74].

In an enlarged Hilbert space, every spin with states $s = 0,1$ is accompanied by an ancilla with states $a = 0,1$. The space is spanned by states $\prod_j |s_j,a_j\rangle$, where j is a lattice site. The Gibbs operator at an inverse temperature β is obtained from its purification $|\psi(\beta)\rangle$ (defined in the enlarged space) by tracing out the ancillas,

$$\rho(\beta) \propto e^{-\beta H} = \mathrm{Tr}_{\mathrm{ancillas}} |\psi(\beta)\rangle\langle\psi(\beta)|. \tag{2}$$

At $\beta = 0$ we choose a product over lattice sites,

$$|\psi(0)\rangle = \prod_j \sum_{s=0,1} |s_j,s_j\rangle, \tag{3}$$

to initialize the imaginary-time evolution

$$|\psi(\beta)\rangle = e^{-\frac{1}{2}\beta H}|\psi(0)\rangle = U(-i\beta/2)|\psi(0)\rangle. \tag{4}$$

The evolution operator $U(\tau) = e^{-i\tau H}$ acts in the Hilbert space of spins. With the initial state (3) Eq. (2) becomes

$$\rho(\beta) \propto U(-i\beta/2)U^\dagger(-i\beta/2). \tag{5}$$

Just like a pure state of spins, the purification can be represented by an iPEPS (see Fig. 1).

III. THE METHOD

We introduce the algorithm in the more general case of thermal-state simulation by imaginary-time evolution of their purification. To be more specific, we use the example of

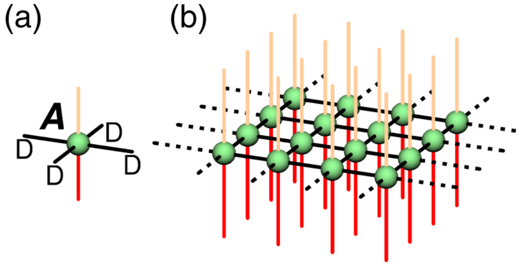

FIG. 1. (a) An elementary rank-6 tensor A of a purification. The top orange index indicates ancilla states $a = 0, 1$, the bottom red index indicates spins states $s = 0, 1$, and the four black bond indices have a bond dimension D. (b) An iPEPS representation of the purification. Here pairs of elementary tensors at NN lattice sites were contracted through their connecting bond indices. The whole network is an amplitude for a joint spin and ancilla state labeled by the spin and ancilla indices. Reducing the dimension of ancilla indices to 1 (or simply ignoring the ancilla lines), we obtain a well-known iPEPS representation of a pure state.

the quantum Ising model. Modification to real-time evolution amounts to ignoring any ancilla lines in the diagrams. For the sake of clarity, in the main text we fully employ the symmetry of the Ising model, but we do our numerical simulations with a more efficient algorithm, described in the Appendix, that breaks the symmetry by applying two-site nearest-neighbor (NN) gates. That algorithm can be generalized to less symmetric models in a straightforward manner.

A. Suzuki-Trotter decomposition

In the second-order Suzuki-Trotter decomposition a small time step is

$$U(d\tau) = U_h(d\tau/2)U_{ZZ}(d\tau)U_h(d\tau/2), \tag{6}$$

where

$$U_{ZZ}(d\tau) = \prod_{\langle j,j'\rangle} e^{id\tau Z_j Z_{j'}}, \quad U_h(d\tau) = \prod_j e^{id\tau h_j} \tag{7}$$

are elementary gates and $h_j = h_x X_j + h_z Z_j$.

In order to rearrange $U(d\tau)$ as a tensor network, we use singular-value decomposition to rewrite a two-site term $e^{id\tau Z_j Z_{j'}}$ acting on a NN bond as a contraction of two smaller tensors acting on a single site:

$$e^{id\tau Z_j Z_{j'}} = \sum_{\mu=0,1} z_{j,\mu} z_{j',\mu}. \tag{8}$$

Here μ is a bond index, and $z_{j,\mu} \equiv \sqrt{\Lambda_\mu}\,(Z_j)^\mu$, $\Lambda_0 = \cos d\tau$, and $\Lambda_1 = i \sin d\tau$. Now we can write

$$U(d\tau) = \sum_{\{\mu\}} \prod_j \left[e^{id\tau h_j/2} \left(\prod_{j'} z_{j,\mu_{\langle j,j'\rangle}} \right) e^{id\tau h_j/2} \right]. \tag{9}$$

Here $\mu_{\langle j,j'\rangle}$ is a bond index on the NN bond $\langle j, j'\rangle$, and $\{\mu\}$ is a collection of all such bond indices. The square brackets enclose a Trotter tensor $T(d\tau)$ at site j [see Fig. 2(a)]. It is a spin operator depending on the bond indices connecting its site to its four NNs. A contraction of these Trotter tensors is the gate $U(d\tau)$ in Fig. 2(b). The evolution operator is a product of such time steps, $U(Nd\tau) = [U(d\tau)]^N$.

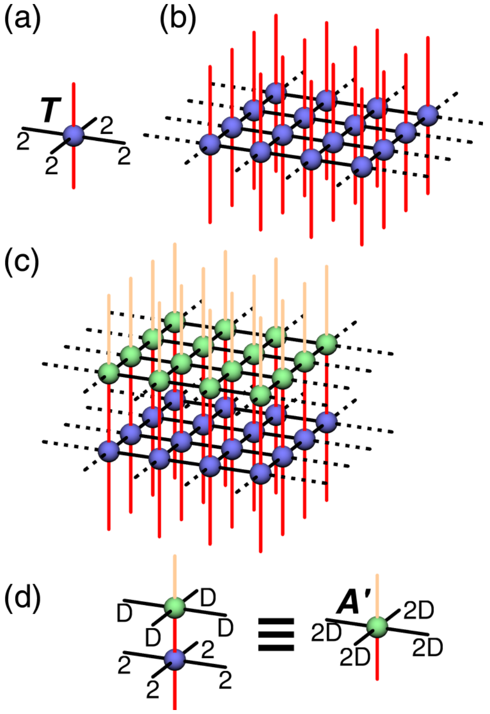

FIG. 2. (a) An elementary rank-6 Trotter tensor T with two red spin indices and four black bond indices, each of dimension 2. (b) A layer of Trotter tensors representing a small time step $U(d\tau)$. (c) The time step $U(d\tau)$ is applied to spin indices of the purification. (d) The tensors T and A can be contracted into a single new tensor A'. A layer of A' makes a new iPEPS that looks like the original one in Fig. 1(b) but has a doubled bond dimension $2D$.

B. Variational truncation

The time step $U(d\tau)$ applied to the state $|\psi\rangle$ yields a new state,

$$|\psi'\rangle = U(d\tau)|\psi\rangle \tag{10}$$

[see Figs. 2(c) and 2(d)]. If $|\psi\rangle$ has a bond dimension D, then the new iPEPS has twice the original bond dimension $2D$.

In order to prevent exponential growth of the dimension in time, the new iPEPS has to be approximated by a more compact one, $|\psi''\rangle$, made of tensors A'' with the original bond dimension D. The best $|\psi''\rangle$ minimizes the norm

$$||\psi''\rangle - |\psi'\rangle|^2. \tag{11}$$

Equivalently, up to normalization of $|\psi''\rangle$, the quality of the approximation can be measured by a global fidelity,

$$F = \frac{\langle\psi''|\psi'\rangle\langle\psi'|\psi''\rangle}{\langle\psi''|\psi''\rangle}. \tag{12}$$

After a rearrangement in Sec. III C, it becomes an efficient figure of merit.

The iPEPS tensor A'', which is the same at all sites, has to be optimized globally. However, the first step towards this global optimum is a local preupdate. We choose site j and label the tensor at this site A''_j. This tensor is optimized while all other tensors are kept fixed as A''. With the last constraint the norm (11) becomes a quadratic form in A''_j. The quadratic form is minimized with respect to A''_j by $\tilde{A}$, which solves the linear equation

$$G\tilde{A} = V. \tag{13}$$

Here

$$G = \frac{\partial^2 \langle \psi'' | \psi'' \rangle}{\partial (A''_j)^* \partial (A''_j)},\ V = \frac{\partial \langle \psi'' | \psi' \rangle}{\partial (A''_j)^*} \tag{14}$$

are, respectively, a metric tensor and a gradient. Further details on the local preupdate can be found in Sec. III D.

The global fidelity (12) is not guaranteed to increase when the local optimum $\tilde{A}$ is substituted globally, i.e., in place of every A'' on every lattice site. However, $\tilde{A}$ can be used as an estimate of the most desired direction of the change in A''. In this vein, we attempt an update

$$A'' = A \cos\epsilon + \tilde{A} \sin\epsilon, \tag{15}$$

with an adjustable parameter $\epsilon \in [-\pi/2, \pi/2]$ using an algorithm proposed in Ref. [31], for which a simplified version was introduced in Refs. [75,76]. This update was successfully used in a similar variational problem of minimizing the energy of an iPEPS as a function of A in Ref. [31], to which we refer the reader for its detailed account. Here we just sketch the general idea.

To begin with, the global fidelity F_0 is calculated for the "old" tensor $A'' = A$ with $\epsilon = 0$. For small ϵ the optimization is prone to get trapped in a local optimum. That is why large $\epsilon = \pi/2$ is tried first, and if $F > F_0$, then $A'' = \tilde{A}$ is accepted. Otherwise, ϵ is halved as many times as necessary for F to increase above F_0, and then $A'' = \tilde{A}$ is accepted. Negative ϵ are also considered in case the global F does not increase for a positive ϵ.

Once A'' in (15) is accepted, the whole procedure, beginning with a solution of (13), is iterated until F is converged. The final converged A'' is accepted as a global optimum.

C. Efficient fidelity computation

In the limit of an infinite lattice, the overlaps in the fidelity (12) become

$$\langle \psi'' | \psi' \rangle = \lim_{N\to\infty} n^N,\ \langle \psi'' | \psi'' \rangle = \lim_{N\to\infty} d^N, \tag{16}$$

where N is the number of lattice sites. Consequently, the fidelity becomes $F = \lim_{N\to\infty} f^N$, where

$$f = \frac{nn^*}{d} \tag{17}$$

is a figure of merit per site.

The factors n and d can be computed by CTMRG [68], generalizing the CTMRG approach to compute a partition function per site for 2D statistical models [65,77–79]. First of all, each overlap, either $\langle \psi'' | \psi' \rangle$ or $\langle \psi'' | \psi'' \rangle$, can be represented by a planar network in Fig. 3(c). With the help of CTMRG [26,65–67], this infinite network can be effectively replaced by a finite one, as shown in Fig. 4. Figure 5 shows how to obtain n and d with the effective environmental tensors introduced in Fig. 4.

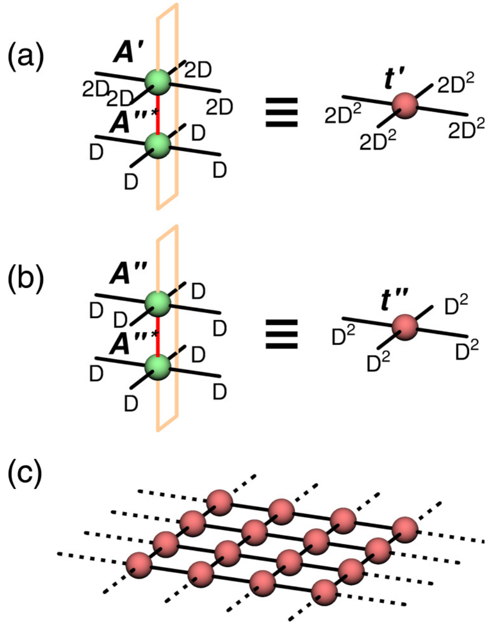

FIG. 3. (a) Tensor A' is contracted with a complex conjugate of A'' into a transfer tensor t' with a bond dimension $d = 2D^2$. (b) Tensor A'' is contracted with its own complex conjugate into a transfer tensor t'' with a bond dimension $d = D^2$. (c) An infinite layer of tensors t' (t'') represents the overlap $\langle \psi'' | \psi' \rangle$ ($\langle \psi'' | \psi'' \rangle$).

D. Local preupdate

In order to construct G and V from the effective environmental tensors C and T, it is useful to note first that a derivative of a contraction of two rank-n tensors $f = \sum_{i_1,\ldots,i_n} A_{i_1,\ldots,i_n} B_{i_1,\ldots,i_n}$ with respect to one of them gives the other one: $\partial f / \partial A_{i_1,\ldots,i_n} = B_{i_1,\ldots,i_n}$. Furthermore, we note that both the optimized tensor A''_j and its conjugate $(A''_j)^*$ are located at the same site j and they enter the overlap $\langle \psi'' | \psi'' \rangle$ ($\langle \psi'' | \psi' \rangle$) only through the tensor t'' (t') defined in Fig. 3(a), located at this site. We distinguish this tensor t'' (t') by an index j and call it t''_j (t'_j). Therefore, the derivatives in Eq. (14)

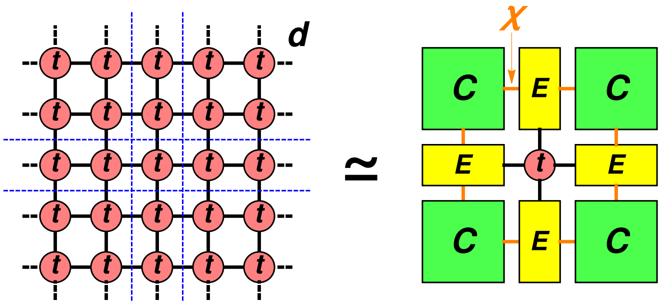

FIG. 4. Left: planar version of Fig. 3(c). Right: its approximate representation with corner tensors C and edge tensors E. Here C effectively represents a corner of the infinite graph on the left, and E is its semi-infinite edge. The environmental bond dimension χ controls the accuracy of the approximation. Tensors C and E are obtained with the corner-transfer-matrix renormalization group [26,65–67].

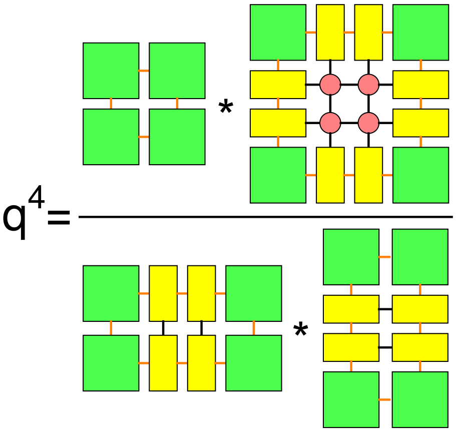

FIG. 5. The environmental tensors introduced in Fig. 4 can be used to calculate the figure of merit (17). This diagram shows a fourth power of a factor q by which the diagram in Fig. 3(c) (or, equivalently, the left panel of Fig. 4) is multiplied when four sites are added to the network. Depending on the overlap in question, either $\langle\psi''|\psi'\rangle$ or $\langle\psi''|\psi''\rangle$ (see Fig. 3), the factor is either $n = q$ or $d = q$, respectively. The diagram is equivalent to Fig. 13.9 in Baxter [77].

decompose into a tensor contraction of derivatives

$$G = \frac{\partial\langle\psi''|\psi''\rangle}{\partial t''_j}\,\frac{\partial^2 t''_j}{\partial(A''_j)^*\partial(A''_j)}, \tag{18}$$

$$V = \frac{\partial\langle\psi''|\psi'\rangle}{\partial t'_j}\,\frac{\partial t'_j}{\partial(A''_j)^*}. \tag{19}$$

The derivatives of the overlaps with respect to t'_j (t''_j) are represented by Fig. 6(a), where one tensor t'_j (t''_j) at site j was removed from the overlap shown in Figs. 3(c) and 4. Indeed, a contraction of the missing t'_j (t''_j) with its environment in Fig. 6(a) through corresponding indices gives back the overlap. Diagramatically, this contraction amounts to filling the hole in Fig. 6(a) with the missing t'_j (t''_j). In numerical calculations, the infinite diagram in Fig. 6(a) is approximated by an equivalent finite one in away similar to that in Fig. 4.

The rank-4 tensor in Fig. 6(a) is a tensor environment for t'_j (t''_j). Each of its four indices is a concatenation of two iPEPS bond indices, one from the ket and one from the bra iPEPS layer, and has a dimension equal to $D \times D$ ($2D \times D$). After splitting each index back into ket and bra indices, this environment can be used to calculate G (V), as shown in Fig. 6(c) [Fig. 6(b)]. In Fig. 6(b) the hole in Fig. 6(a) (with split ket and bra indices) is filled with the second derivative of t''_j with respect to A''_j and $(A''_j)^*$. Similar to the derivative of an overlap with respect to t''_j, this derivative is obtained from the tensor t''_j in Fig. 3(b) by removing both A''_j and $(A''_j)^*$ from the diagram. In Fig. 6(c) the hole in Fig. 6(a) is filled by the derivative of t'_j with respect to $(A''_j)^*$. This derivative is obtained from the tensor t'_j in Fig. 3(a) by removing $(A''_j)^*$ from the diagram.

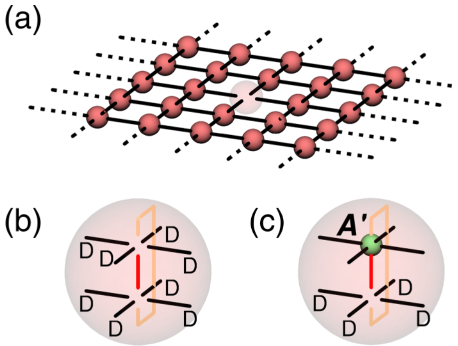

FIG. 6. (a) Tensor environment for t' (t''). It is obtained by removing one tensor t' (t'') from the overlap in Fig. 3(c) or, equivalently, from the right diagram in Fig. 4. The environment represents a derivative of the overlap $\langle\psi''|\psi'\rangle$ ($\langle\psi''|\psi''\rangle$) with respect to t' (t''); see Eqs. (18) and (19). This rank-4 tensor has four indices with dimension $D \times 2D$ ($D \times D$). (b) In the case of t'' [Eq. (18)] each of the four indices in (a) is decomposed back into two indices, each of dimension D. The diagram represents the metric tensor G. The red spin line is a Kronecker δ for spin states and the orange ancilla line is a delta for ancillas. Therefore, the metric can be decomposed as $G = g \otimes 1_s \otimes 1_a$, where g is the tensor environment for t. (c) In the case of t' (19) each of the four indices in (a) is decomposed back into two indices of dimension $2D$ (top) and D (bottom). After contracting the upper indices with A' the diagram becomes the gradient V.

We have to keep in mind that the environmental tensors are converged with limited precision that is usually set by demanding that local observables are converged with precision $\simeq 10^{-8}$. This precision limits the accuracy to which the matrix G is Hermitian and positive definite. In order to avoid numerical instabilities this error has to be filtered out by eliminating the anti-Hermitian part of G and then truncating its eigenvalues that are less than a fraction of its maximal eigenvalue. The fraction is usually set at 10^{-8}. To this end we solve the linear equation (13) using the Moore-Penrose pseudoinverse

$$\tilde{A} = \mathrm{pinv}(G)V, \tag{20}$$

where the truncation is implemented by setting an appropriate tolerance in the pseudoinverse procedure.

Another advantage of the pseudoinverse solution is that it does not contain any zero modes of G. By definition, these zero modes do not matter for the local optimization problem, but they can make futile the attempt in (15) to use $\tilde{A}$ as a significant part of the global solution.

A possibility of further simplification occurs in Fig. 6(b), where the open spin and ancilla lines represent two Kronecker symbols. The symbols are identities in the spin and ancilla subspace, and therefore, the metric G has a convenient tensor-product structure $G = g \otimes 1_s \otimes 1_a$, where g is a reshaped tensor environment for t''_j and 1_s and 1_a are identities for spins and ancillas, respectively. Therefore, after appropriate reshaping of tensors, Eq. (20) can be reduced to

$$\tilde{A} = \mathrm{pinv}(g)V, \tag{21}$$

where only the small tensor environment g has to be pseudoinverted.

IV. THERMAL STATES FROM IMAGINARY-TIME EVOLUTION

In this section we present results obtained by imaginary-time evolution for two values of the transverse field, $h_x = 2.5$ and $h_x = 2.9$ (see Figs. 7 and 8), corresponding to critical

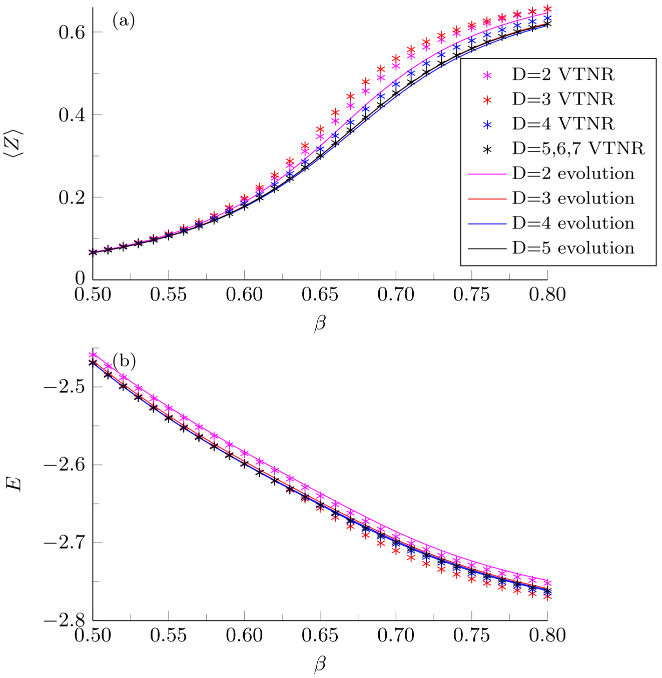

FIG. 7. Thermal states for a transverse field $h_x = 2.5$ with a longitudinal bias $h_z = 0.01$. The stars are results from variational tensor network renormalization (VTNR), and the solid lines are from the imaginary-time evolution. With increasing bond dimension D the two methods converge on each other. (a) Longitudinal magnetization $\langle Z\rangle$ as a function of inverse temperature. (b) Energy per site E as a function of inverse temperature.

temperatures $\beta_c = 0.7851(4)$ and $\beta_c = 1.643(2)$, respectively [80]. We show data with $D = 2,3,4,5$. The stronger field is closer to the quantum critical point at h_0; hence, quantum fluctuations are stronger, and a bigger bond dimension D is required for convergence. For the evolution to run smoothly across the critical point we added a small longitudinal bias, $h_z = 0.01$.

Figures 7(a) and 7(b) show the longitudinal magnetization $\langle Z\rangle$ and energy E for the two transverse fields. The data from the evolution are compared to results obtained with the VTNR [35,43–45]. With increasing D each of the two methods converges, and they converge with each other. This is a proof of principle that the variational time evolution can be applied to thermal states.

The data at hand suggest that with increasing D the evolution converges faster than VTNR. However, at least for the Ising benchmark, the numerical effort necessary to obtain results of similar accuracy is roughly the same. In both methods the bottleneck is the corner-transfer-matrix renormalization procedure. In the case of VTNR larger D is necessary, but in the case of the evolution the environmental tensors need to be computed more times.

The advantage of VTNR is that it targets the desired temperature directly; there is no need to evolve from $\beta = 0$, and thus no evolution errors are accumulated. In order to minimize the accumulation when evolving across the critical regime, a small longitudinal bias has to be applied. The critical singularity is recovered in the limit of small bias that requires large D.

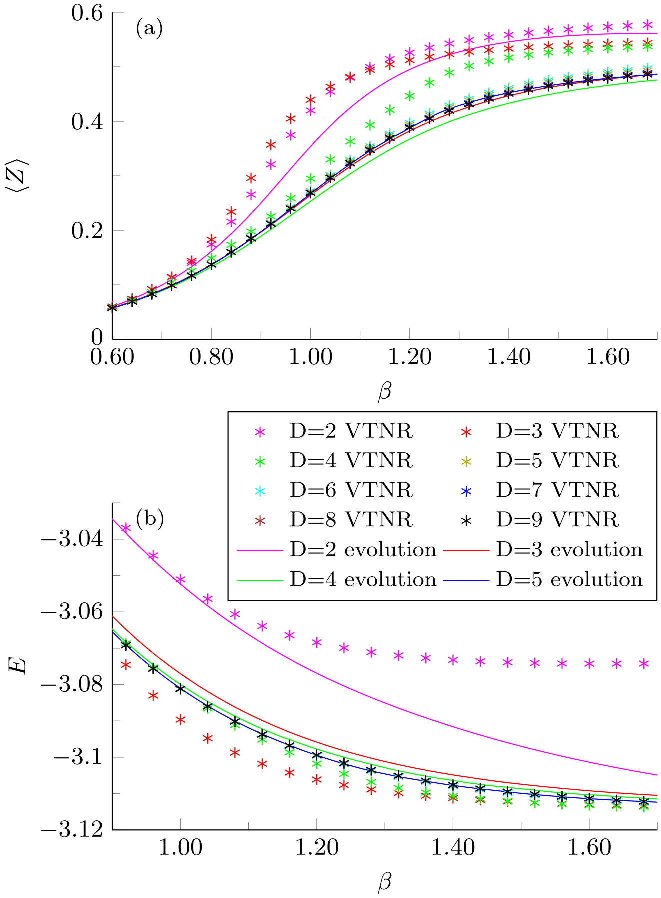

FIG. 8. Thermal states for a transverse field $h_x = 2.9$ with a longitudinal bias $h_z = 0.01$. The stars are results from variational tensor network renormalization (VTNR), and the solid lines are from the imaginary-time evolution. With increasing bond dimension D the two methods converge on each other. (a) Longitudinal magnetization $\langle Z\rangle$ as a function of inverse temperature. (b) Energy per site E as a function of inverse temperature.

However, one big advantage of the variational evolution is that unlike VTNR targeting the accuracy of the partition function, it aims directly at an accurate thermal state. In some models this may prove to be a major advantage.

V. TIME EVOLUTION AFTER A SUDDEN QUENCH

Next, we move to the simulation of a real-time evolution after a quench in an unbiased model (1) with $h_z = 0$. The initial state is the ground state for $h_x \gg h_0$ with all spins pointing along x. At $t = 0$ the Hamiltonian is suddenly quenched down to finite $h_x = 2h_0, h_0, h_0/10$, which are, respectively, above, at, and below the quantum critical point h_0.

Figure 9 shows a time evolution of the magnetization $\langle X\rangle$ and energy per site E after the sudden quench for bond dimensions $D = 2,3,4$. With increasing D the energy becomes conserved more accurately for a longer time. This is an indication of the general convergence of the algorithm.

Not surprisingly, the results are most accurate for $h_x = h_0/10$. This weak transverse field is close to $h_x = 0$ when the Hamiltonian is classical and the time evolution can be represented exactly with $D = 2$. At $h_x = 0$ quasiparticles

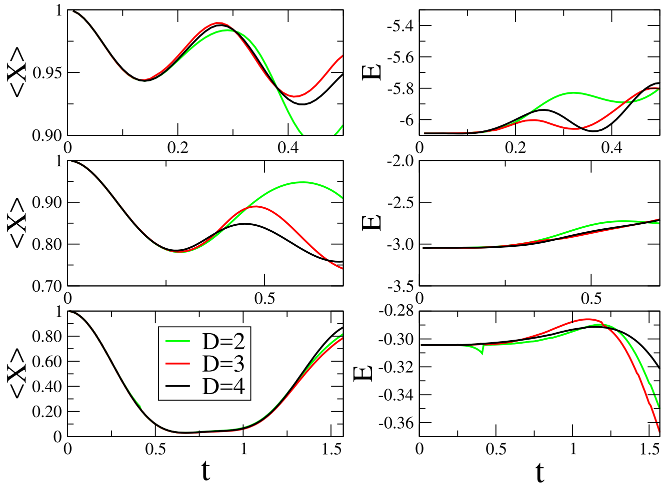

FIG. 9. Transverse magnetization $\langle X\rangle$ (left column) and energy per site (right column) after a sudden quench from a ground state in a strong transverse field, $h_x \gg h_0$, with all spins pointing along x down to a finite $h_x = 2h_0$ (top row), $h_x = h_0$ (middle row), and $h_x = h_0/10$ (bottom row). The quench is, respectively, within the same phase, to the quantum critical point, and to a different phase. Energy conservation shows systematic improvement with increasing bond dimension $D = 2,3,4$. We see that for sufficiently small times seemingly converged results for transverse magnetization can be obtained. While approaching the limit of small entanglement ($h_x = h_0/10$), we see that the convergence time is growing longer, as expected.

have a flat dispersion relation and do not propagate; hence, even though they are excited as entangled pairs with opposite quasimomenta, they do not spread entanglement across the system. For any $h_x > 0$, however, the entanglement grows with time, and any bond dimension is bound to become insufficient after a finite evolution time. However, as discussed in Sec. I, there are potential applications where this effect is of limited importance.

VI. CONCLUSION

We tested a straightforward algorithm to simulate real- and imaginary-time evolution with infinite iPEPS. The algorithm is based on variational maximization of the fidelity between a new iPEPS obtained after direct application of a time step and its approximation by an iPEPS with the original bond dimension.

The main result is the simulation of real-time evolution after a sudden quench of a Hamiltonian. With increasing bond dimension the results converge over increasing evolution time. This is a proof-of-principle demonstration that simulation of real-time evolution with a 2D tensor network is feasible.

We also applied the same algorithm to evolve purification of thermal states. These results converge to the established VTNR method, providing a proof of principle that the algorithm can be applied to 2D strongly correlated systems at finite temperature.

ACKNOWLEDGMENTS

P.C. acknowledges inspiring discussions with P. Corboz on application of CTMRG to the calculation of the partition function per site and simulations of thermal states. We thank S. Wessel for numerical values of data published in Ref. [80]. Simulations were done with extensive use of the NCON function [81]. This research was funded by the National Science Center, Poland, under project 2016/23/B/ST3/00830 (P.C.) and National Science Center, Poland and European Union under Quantera project 2017/25/Z/ST2/03028 (J.D.).

APPENDIX: TWO-SITE GATES

For the sake of clarity, the main text presents a straightforward single-site version of the algorithm. In practice it is more efficient to implement the gate $U_{ZZ}(d\tau)$ as a product of two-site gates. To this end the infinite square lattice is divided into two sublattices, A and B [see Fig. 10(a)]. On the checkerboard the gate becomes a product,

$$U_{ZZ}(d\tau) = U_0^a(d\tau)U_1^a(d\tau)U_0^b(d\tau)U_1^b(d\tau). \quad \text{(A1)}$$

Here a and b are the Cartesian lattice directions spanned by e_a and e_b,

$$U_s^a(d\tau) = \prod_{mn} e^{id\tau Z_{2m+s-1,n} Z_{2m+s,n}}, \quad \text{(A2)}$$

$$U_s^b(d\tau) = \prod_{mn} e^{id\tau Z_{m,2n+s-1} Z_{m,2n+s}}, \quad \text{(A3)}$$

and $Z_{m,n}$ is an operator at site $me_a + ne_b$.

Every NN gate in (A2) and (A3) is decomposed as in (8). Consequently, when a gate, say, $U_0^a(d\tau)$, is applied to the checkerboard AB iPEPS in Fig. 10(a), then every pair of tensors A and B at every pair of NN sites $(2m-1)e_a + ne_b$ and $2me_a + ne_b$ is applied with the NN gate's decomposition as in Fig. 10(b). When the tensors A and B are fused with their respective z, they become A' and B', respectively, which are connected by an index with a bond dimension $2D$ [see Fig. 10(c)].

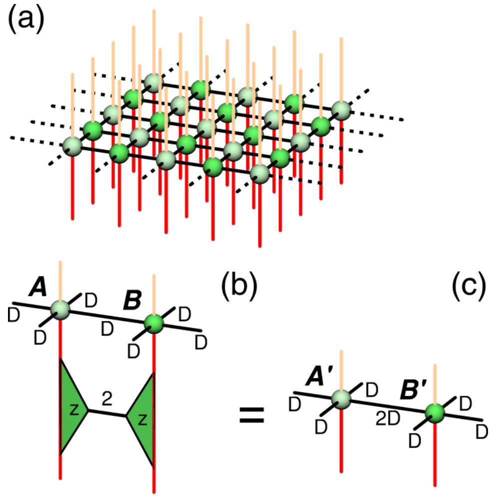

FIG. 10. (a) The infinite square lattice is divided into two sublattices with tensors A (lighter green) and B (darker green). (b) SVD decomposition of a NN gate is applied to every pair A and B of NN tensors. (c) When the tensors A and B are contracted with their respective z, they become new tensors A' and B' with a doubled bond dimension $2D$ on their common NN bond. By variational optimization the iPEPS made of A' and B' is approximated by a new iPEPS made of A'' and B'' with the original bond dimension D.

The action of the gate $U_0^a(d\tau)$ is completed when the $A'B'$ iPEPS is approximated by a (variationally optimized) new $A''B''$ iPEPS with the original bond dimension D at every bond.

Apart from the opportunity to use reduced tensors in the variational optimization, the main advantage of the two-site gates is that the enlarged bond dimension $2D$ appears only on a minority of bonds. This speeds up the CTMRG for the overlap $\langle\psi'|\psi''\rangle$, which is the most time-consuming part of the algorithm. The decomposition into two-site gates breaks the symmetry of the lattice. Therefore, we use the efficient nonsymmetric version of CTMRG [67] for the checkerboard lattice.

[1] F. Verstraete, V. Murg, and J. Cirac, Adv. Phys. **57**, 143 (2008).

[2] R. Orús, Ann. Phys. (NY) **349**, 117 (2014).

[3] M. Fannes, B. Nachtergaele, and R. F. Werner, Commun. Math. Phys. **144**, 443 (1992).

[4] F. Verstraete and J. I. Cirac, arXiv:cond-mat/0407066.

[5] M. B. Hastings, J. Stat. Mech. (2007) P08024.

[6] N. Schuch, M. M. Wolf, F. Verstraete, and J. I. Cirac, Phys. Rev. Lett. **100**, 030504 (2008).

[7] T. Barthel, arXiv:1708.09349.

[8] S. R. White, Phys. Rev. Lett. **69**, 2863 (1992).

[9] S. R. White, Phys. Rev. B **48**, 10345 (1993).

[10] U. Schollwöck, Rev. Mod. Phys. **77**, 259 (2005).

[11] U. Schöllwock, Ann. Phys. (NY) **326**, 96 (2011).

[12] A. Molnar, N. Schuch, F. Verstraete, and J. I. Cirac, Phys. Rev. B **91**, 045138 (2015).

[13] Y. Ge and J. Eisert, New J. Phys. **18**, 083026 (2016).

[14] C. Pineda, T. Barthel, and J. Eisert, Phys. Rev. A **81**, 050303 (2010).

[15] P. Corboz and G. Vidal, Phys. Rev. B **80**, 165129 (2009).

[16] T. Barthel, C. Pineda, and J. Eisert, Phys. Rev. A **80**, 042333 (2009).

[17] Z.-C. Gu, F. Verstraete, and X.-G. Wen, arXiv:1004.2563.

[18] C. V. Kraus, N. Schuch, F. Verstraete, and J. I. Cirac, Phys. Rev. A **81**, 052338 (2010).

[19] P. Corboz, R. Orús, B. Bauer, and G. Vidal, Phys. Rev. B **81**, 165104 (2010).

[20] P. Corboz, S. R. White, G. Vidal, and M. Troyer, Phys. Rev. B **84**, 041108 (2011).

[21] V. Murg, F. Verstraete, and J. I. Cirac, Phys. Rev. A **75**, 033605 (2007).

[22] Y. Nishio, N. Maeshima, A. Gendiar, and T. Nishino, arXiv:cond-mat/0401115.

[23] J. Jordan, R. Orús, G. Vidal, F. Verstraete, and J. I. Cirac, Phys. Rev. Lett. **101**, 250602 (2008).

[24] H. C. Jiang, Z. Y. Weng, and T. Xiang, Phys. Rev. Lett. **101**, 090603 (2008).

[25] Z.-C. Gu, M. Levin, and X.-G. Wen, Phys. Rev. B **78**, 205116 (2008).

[26] R. Orús and G. Vidal, Phys. Rev. B **80**, 094403 (2009).

[27] Y. H. Matsuda, N. Abe, S. Takeyama, H. Kageyama, P. Corboz, A. Honecker, S. R. Manmana, G. R. Foltin, K. P. Schmidt, and F. Mila, Phys. Rev. Lett. **111**, 137204 (2013).

[28] P. Corboz and F. Mila, Phys. Rev. Lett. **112**, 147203 (2014).

[29] B.-X. Zheng, C.-M. Chung, P. Corboz, G. Ehlers, M.-P. Qin, R. M. Noack, H. Shi, S. R. White, S. Zhang, and G. K.-L. Chan, Science **358**, 1155 (2017).

[30] H. J. Liao, Z. Y. Xie, J. Chen, Z. Y. Liu, H. D. Xie, R. Z. Huang, B. Normand, and T. Xiang, Phys. Rev. Lett. **118**, 137202 (2017).

[31] P. Corboz, Phys. Rev. B **94**, 035133 (2016).

[32] L. Vanderstraeten, J. Haegeman, P. Corboz, and F. Verstraete, Phys. Rev. B **94**, 155123 (2016).

[33] M. T. Fishman, L. Vanderstraeten, V. Zauner-Stauber, J. Haegeman, and F. Verstraete, arXiv:1711.05881.

[34] Z. Y. Xie, H. J. Liao, R. Z. Huang, H. D. Xie, J. Chen, Z. Y. Liu, and T. Xiang, Phys. Rev. B **96**, 045128 (2017).

[35] P. Czarnik, M. M. Rams, and J. Dziarmaga, Phys. Rev. B **94**, 235142 (2016).

[36] P. Corboz, Phys. Rev. B **93**, 045116 (2016).

[37] P. Corboz, P. Czarnik, G. Kapteijns, and L. Tagliacozzo, arXiv:1803.08445.

[38] M. Rader and A. M. Läuchli, arXiv:1803.08566.

[39] M. M. Rams, P. Czarnik, and L. Cincio, arXiv:1801.08554.

[40] P. Czarnik, L. Cincio, and J. Dziarmaga, Phys. Rev. B **86**, 245101 (2012).

[41] P. Czarnik and J. Dziarmaga, Phys. Rev. B **90**, 035144 (2014).

[42] P. Czarnik and J. Dziarmaga, Phys. Rev. B **92**, 035120 (2015).

[43] P. Czarnik, J. Dziarmaga, and A. M. Oleś, Phys. Rev. B **93**, 184410 (2016).

[44] P. Czarnik and J. Dziarmaga, Phys. Rev. B **92**, 035152 (2015).

[45] P. Czarnik, J. Dziarmaga, and A. M. Oleś, Phys. Rev. B **96**, 014420 (2017).

[46] Y.-W. Dai, Q.-Q. Shi, S. Y. Cho, M. T. Batchelor, and H.-Q. Zhou, Phys. Rev. B **95**, 214409 (2017).

[47] A. Kshetrimayum, H. Weimer, and R. Orús, Nat. Commun. **8**, 1291 (2017).

[48] L. Vanderstraeten, M. Mariën, F. Verstraete, and J. Haegeman, Phys. Rev. B **92**, 201111 (2015).

[49] W. Li, S.-J. Ran, S.-S. Gong, Y. Zhao, B. Xi, F. Ye, and G. Su, Phys. Rev. Lett. **106**, 127202 (2011).

[50] Z. Y. Xie, J. Chen, M. P. Qin, J. W. Zhu, L. P. Yang, and T. Xiang, Phys. Rev. B **86**, 045139 (2012).

[51] S.-J. Ran, W. Li, B. Xi, Z. Zhang, and G. Su, Phys. Rev. B **86**, 134429 (2012).

[52] S.-J. Ran, B. Xi, T. Liu, and G. Su, Phys. Rev. B **88**, 064407 (2013).

[53] S.-J. Ran, W. Li, S.-S. Gong, A. Weichselbaum, J. von Delft, and G. Su, Phys. Rev. B **97**, 075146 (2018).

[54] C. Peng, S.-J. Ran, T. Liu, X. Chen, and G. Su, Phys. Rev. B **95**, 075140 (2017).

[55] X. Chen, S.-J. Ran, T. Liu, C. Peng, Y.-Z. Huang, and G. Su, arXiv:1711.01001.

[56] G. Vidal, Phys. Rev. Lett. **99**, 220405 (2007).

[57] G. Vidal, Phys. Rev. Lett. **101**, 110501 (2008).

[58] G. Evenbly and G. Vidal, Phys. Rev. Lett. **112**, 220502 (2014).

[59] G. Evenbly and G. Vidal, Phys. Rev. B **89**, 235113 (2014).

[60] B. Bruognolo, Z. Zhu, S. R. White, and E. M. Stoudenmire, arXiv:1705.05578.

[61] B.-B. Chen, L. Chen, Z. Chen, W. Li, and A. Weichselbaum, arXiv:1801.00142.

[62] H. F. Trotter, Proc. Am. Math. Soc. **10**, 545 (1959).

[63] M. Suzuki, J. Phys. Soc. Jpn. **21**, 2274 (1966).

[64] M. Suzuki, Prog. Theor. Phys. **56**, 1454 (1976).

[65] R. J. Baxter, J. Stat. Phys. **19**, 461 (1978).

[66] T. Nishino and K. Okunishi, J. Phys. Soc. Jpn. **65**, 891 (1996).

[67] P. Corboz, T. M. Rice, and M. Troyer, Phys. Rev. Lett. **113**, 046402 (2014).

[68] S. S. Jahromi, R. Orús, M. Kargarian, and A. Langari, Phys. Rev. B **97**, 115161 (2018).

[69] J. C. Halimeh and V. Zauner-Stauber, Phys. Rev. B **96**, 134427 (2017).

[70] L. Cincio, J. Dziarmaga, M. M. Rams, and W. H. Zurek, Phys. Rev. A **75**, 052321 (2007).

[71] T. B. Wahl, A. Pal, and S. H. Simon, arXiv:1711.02678.

[72] A. H. Werner, D. Jaschke, P. Silvi, M. Kliesch, T. Calarco, J. Eisert, and S. Montangero, Phys. Rev. Lett. **116**, 237201 (2016).

[73] M. M. Wolf, F. Verstraete, M. B. Hastings, and J. I. Cirac, Phys. Rev. Lett. **100**, 070502 (2008).

[74] H. W. J. Blöte and Y. Deng, Phys. Rev. E **66**, 066110 (2002).

[75] T. Nishino, Y. Hieida, K. Okunishi, N. Maeshima, Y. Akutsu, and A. Gendiar, Prog. Theor. Phys. **105**, 409 (2001).

[76] A. Gendiar, N. Maeshima, and T. Nishino, Prog. Theor. Phys. **110**, 691 (2003).

[77] R. J. Baxter, *Exactly Solved Models in Statistical Mechanics* (Academic Press, London, 1982).

[78] Y.-b. Chan, J. Phys. A **45**, 085001 (2012).

[79] Y.-b. Chan, J. Phys. A **46**, 125009 (2013).

[80] S. Hesselmann and S. Wessel, Phys. Rev. B **93**, 155157 (2016).

[81] R. N. C. Pfeifer, G. Evenbly, S. Singh, and G. Vidal, arXiv:1402.0939.